SASA: Super-resolution and Ambiguity-free Sparse Array Geometry Optimization with Aperture Size Constraints for MIMO Radar

Mingsai Huan, Junli Liang, *Senior Member, IEEE*, Yifan Wu, Yongkang Li, Wei Liu, *Senior Member, IEEE*

Abstract—To improve the performance of multiple-input-multiple-output (MIMO) radar, various sparse arrays have been employed. However, the angular resolution of existing non-uniform arrays optimized by either combinatorial algorithms or heuristic ones is limited by the Rayleigh criterion, which is strictly related to the aperture size. Based on the angular ambiguity function (AAF) analysis, two new models are established in this work for directly optimizing the sidelobe level (SLL) or the main lobe width (MLW) with the constraints of aperture size and element spacing. The aforementioned designs result in non-convex and nonlinear optimization problems, and solutions are derived via the alternating direction multiplier method (ADMM). Furthermore, considering a parametric trade-off between SLL and MLW, a hybrid algorithm is proposed to search for the SLL-MLW Pareto front boundary. Finally, simulations are provided to demonstrate the high angular resolution and ambiguity-free properties of the optimized sparse arrays.

Index Terms—MIMO radar, sparse array, angular ambiguity function, non-convex optimization, angular resolution.

I. INTRODUCTION

MIMO radar [1] has a wide range of applications such as autonomous driving with automotive radar [2], [3], and assisted living [4], including monitoring of vital signs, fall detection, gesture recognition, etc. The next-generation MIMO radar sensors are expected to have a finer imaging capability so that more details can be acquired from the point cloud, which is beneficial for subsequent vehicle detection and human motion recognition. Both automotive radar and indoor radar demand high resolution, high dynamic range, low latency, low hardware cost, and small size.

To improve the performance of direction of arrival (DoA) estimation, a large number of super-resolution DoA estimation methods have been proposed such as MUSIC [5] and IAA [6], but it is difficult to implement some of them in practice due to their high computational complexity. Given its low complexity and high resolution, non-uniform arrays for MIMO radar have received a significant amount of attention recently. They can be

divided into two categories: thinned arrays and sparse arrays [7].

Thinned arrays, which are usually optimized by combinatorial optimization algorithms, are formed by selecting a certain number of antenna units from a uniform array, and their element spacings are usually integer multiples of half wavelength. For example, the Texas Instruments AWR1243P imaging radar [8] employs a uniform array in the horizontal direction and a minimum redundant array (MRA) [9] in the elevation direction. The MRA enlarges the aperture size and improves the angular resolution, but it causes angular ambiguity and requires multiple snapshots or additional array elements to estimate the covariance matrix. Considering that only a few snapshots or even a single snapshot is available for 4D imaging radar after range-Doppler two-dimensional fast Fourier transform (2D-FFT), we could use spatial smoothing to generate multiple snapshots, but at the cost of reducing the number of effective array elements and signal-to-noise ratio (SNR) [2], [10]. Therefore, It is still difficult for thinned arrays to meet the high-resolution, ambiguity-free, low-latency, and low-cost requirements for radar products at the same time.

On the other hand, sparse arrays have arbitrarily distributed elements on the antenna aperture. This means that the array elements are not constrained to lay on a regular grid, so the degrees of freedom (DoFs) for optimizing the array geometry become greater. The advantage is that it can reduce the SLL of the pattern, and further improve the performance of DoA estimation. In 2009, nonuniform sparse antenna arrays and MIMO techniques are employed to improve the angular resolution of the proposed frequency-modulated continuous-wave (FMCW) radar system [11]. Because there is no analytical solution to determine the antenna locations that achieve a minimum SLL for a given number of antennas, the element positions and weights are optimized via brute force, stepwise brute force, and particle swarm optimization (PSO) [12].

As a very effective tool for ambiguity characterization of arbitrary antenna arrays, the ambiguity I function [13] becomes one of the focuses in antennas and propagation field, such as [14]–[18]. To distinguish it from the range-Doppler ambiguity function, it is called angular ambiguity function (AAF) in this paper. In [14] and [15], to achieve a better DoA accuracy without angular ambiguity, the SLL of AAF and the Cramér-Rao bound (CRB) are used as metrics to optimize the array geometry. Considering an observation model with a random target phase and known SNR, a constrained optimal design method using the Weiss-Weinstein bound is proposed in [19],

while a genetic algorithm (GA) [16], [17] is used to search for the optimal antenna placement by maximizing the area of the ambiguity-free region defined by AAF. Furthermore, the latter method is extended to the 2-D MIMO array in [18]. Some other methods are also proposed to jointly design the positions and weights of the array elements [20]–[23]. We notice that most authors still employ GA, PSO, and other heuristic algorithms to design a non-uniform array with great effort. Under the constraints of array element spacing, heuristic algorithms have to filter the solutions at each iteration, which leads to decrease in both accuracy and speed. Moreover, it is worth noting that the SLL and MLW are usually trade-offs to be made in the optimization, as illustrated by studies in [22], [24]. Their objective functions often contain multiple metrics weighted together, like αSLL + βMLW, essentially turning the constrained optimization problem into an unconstrained one, which can then be readily solved by heuristic algorithms. Obviously, it involves a lot of efforts to adjust the weighting coefficients α and β to get a more satisfactory solution. Since the weighting method cannot precisely control one of the key metrics, i.e. SLL or MLW, the Pareto optimal solution cannot be found in a single optimization process [24].

Unlike the common heuristic algorithms, our previous work [25]–[27] has demonstrated the distinct decomposition–coordination procedure and superior convergence property of ADMM [28], and utilized the ADMM to derive a optimal solution with a minimum SLL for beampattern synthesis or a minimum CRLB for targets localization. The main issue in this paper when dealing with the design of sparse array geometry is that the optimization of the element positions turns out to be a strongly nonlinear problem since the variables are present in exponential terms [7]. Moreover, in the numerical algorithm of previous studies, the MLW is usually controlled indirectly by setting the sidelobe region [29], and it has never been placed in the objective function due to the complexity of non-convex optimization problems. However, according to [30], a small MLW may be more important than a low SLL for the performance of DOA estimation. From the theory of antennas and array signal processing, it is well known that the angular resolution properties are directly related to the array aperture size according to the Rayleigh criterion [31]. Nevertheless, for sparse arrays with equal aperture size, the MLW may vary due to differences in the distribution of antenna positions [32], which results in differences in the angular resolution. Therefore, numerical algorithms for MLW reduction with multiple constraints will be developed in this paper.

This paper focuses on **s**uper-resolution and **a**mbiguity-free **s**parse **a**rray optimization with aperture size and element spacing constraints for MIMO radar (SASA), with corresponding solutions derived. The main contributions of this paper are as follows:

1) To avoid angular ambiguity and improve the dynamic range [2], a model for optimizing the SLL of the MIMO array AAF under the constraints of aperture size and minimum element spacing is formulated. Unlike existing heuristic algorithms, we utilize the ADMM [28] to derive a solution to such a non-convex and nonlinear problem

by dividing the difficult problem into several solvable subproblems respectively with fewer variables.

2) To improve the angular resolution with a constant dynamic range, this paper develops a novel model for directly optimizing the MLW of the MIMO array AAF under the constraints of SLL, aperture size and element spacing. Then, the non-convex and nonlinear problem is solved iteratively based on the Lagrange multiplier method.

3) Inspired by a two-step method for getting the fixed value of the SLL and minimum desired first null beam width (FNBW) [33], we try to combine the global optimization capability of heuristic algorithms with the accuracy of numerical optimization algorithms and make a parametric trade-off between the SLL and MLW. As a result, a hybrid algorithm with modified real genetic algorithm (MGA) [34] and non-convex optimization algorithms is proposed without setting too many parameters for the optimization problem, with most of the results located on the Pareto front boundary. Furthermore, it is shown that the optimal sparse array improves the performance of DoA estimation. To our best knowledge, this is the first time to show that the angular resolution of sparse arrays with equal aperture size may exceed that of uniform arrays when common DoA estimation methods are employed.

The rest of this paper is organized as follows. Analysis of the angular ambiguity function, expanded beam pattern, antenna position constraints and problem definition are introduced in Section II. The algorithms are developed in Section III. In Section IV, simulations are provided to evaluate the performance of the developed algorithms. Finally, conclusions are drawn in Section V.

Notation: Vectors and matrices are denoted by boldface lowercase and uppercase letters, respectively. $\|\cdot\|$ denotes the Frobenius norm, while $(\cdot)^T$ and $(\cdot)^{-1}$ are the transpose and matrix inverse operators, respectively. $\mathbf{0}_{m \times n}$ and $\boldsymbol{I}_n$ represent the $m \times n$ zero matrix and $n \times n$ identity matrix, respectively. $\Re\{\}$ and $\Im\{\}$ represent the real and imaginary parts with $j = \sqrt{-1}$. $|\cdot|$ and $\angle\{\cdot\}$ are the magnitude and phase of a complex-valued scalar, respectively. $\odot$ represents the Hadamard product. $\otimes$ represents the Kronecker product. $\succeq$ is a type of generalized inequalities, and $\boldsymbol{x} \succeq 0$ means that each element in the vector is greater than 0.

II. PROBLEM DEFINITION

A. Angular Ambiguity Function (AAF)

Consider a collocated MIMO radar system with M transmitting antennas and N receiving antennas. Let $\boldsymbol{t} = [t_1, \ldots, t_M]^T$ and $\boldsymbol{r} = [r_1, \ldots, r_N]^T$ describe the positions of the M transmitters and N receivers, respectively. They are the electrical lengths with respect to the free space wavelength λ_0. Under the narrow-band and far-field condition, the incident signal can be considered as a plane wave. Then, to take into account the radiation property of the antennas, the transmitter and receiver

steering vectors associated with the off-boresight angle θ can be multiplied by the complex antenna radiation pattern [16]

$$\boldsymbol{a}_t(\theta) = \boldsymbol{g}_t(\theta) \odot e^{-j2\pi\boldsymbol{t}\sin\theta},$$
$$\boldsymbol{a}_r(\theta) = \boldsymbol{g}_r(\theta) \odot e^{-j2\pi\boldsymbol{r}\sin\theta}. \quad (1)$$

where $\boldsymbol{g}_t(\theta)$ and $\boldsymbol{g}_r(\theta)$ are the complex vectors of the radiation patterns for a certain polarization of the transmitting and receiving antenna elements in the azimuth plane [35]

$$\boldsymbol{g}_t(\theta) = [g_{t,1}(\theta) \; g_{t,2}(\theta) \; \cdots \; g_{t,M}(\theta)]^T,$$
$$\boldsymbol{g}_r(\theta) = [g_{r,1}(\theta) \; g_{r,2}(\theta) \; \cdots \; g_{r,N}(\theta)]^T. \quad (2)$$

The radiation patterns may differ from element to element because of the mutual coupling effects. Therefore, the average element pattern $\bar{g}(\theta)$ [36], which includes the information on the mutual coupling environment, can be exploited to approximate each element pattern in the array with high accuracy. Then, (1) can be rewritten as

$$\boldsymbol{a}_t(\theta) = \bar{g}(\theta)e^{-j2\pi\boldsymbol{t}\sin\theta},$$
$$\boldsymbol{a}_r(\theta) = \bar{g}(\theta)e^{-j2\pi\boldsymbol{r}\sin\theta}. \quad (3)$$

Multiple virtual channels are created in MIMO radar by transmitting orthogonal waveforms [1]. The virtual array steering vector can be expressed as the Kronecker product of the transmitting and receiving steering vectors, i.e.,

$$\boldsymbol{a}(\theta) = \boldsymbol{a}_t(\theta) \otimes \boldsymbol{a}_r(\theta) = \bar{g}^2(\theta)e^{j2\pi\boldsymbol{Bd}\sin\theta}, \quad (4)$$

where

$$\boldsymbol{B} = \begin{bmatrix} \boldsymbol{I}_{M\times M} \otimes \boldsymbol{1}_{N\times 1} & \boldsymbol{1}_{M\times 1} \otimes \boldsymbol{I}_{N\times N} \end{bmatrix}. \quad (5)$$

The combined element position vector $\boldsymbol{d}$ is defined as

$$\boldsymbol{d} = [\boldsymbol{t}^T, \boldsymbol{r}^T]^T. \quad (6)$$

The ability of the array to discriminate between targets from two different directions is measured by the cosine similarity of the steering vectors corresponding to the two directions, which is called angular ambiguity function (AAF) [13], [16], denoted by

$$AAF(\theta_i, \theta_j) = \frac{\boldsymbol{a}(\theta_j)^H \boldsymbol{a}(\theta_i)}{\|\boldsymbol{a}(\theta_j)\| \|\boldsymbol{a}(\theta_i)\|}$$
$$= \frac{1}{MN} \sum_{m=1}^{M} \sum_{n=1}^{N} e^{j2\pi(t_m+r_n)(\sin\theta_i - \sin\theta_j)}, \quad (7)$$

The AAF after simplification eliminates the effect of element patterns. Although it has almost the same mathematical expression as the array factor of equal-amplitude (also referred to as isophoric like [37]) aperiodic arrays, which can be calculated as

$$ArrayFactor(\theta) = \frac{1}{\tilde{N}} \sum_{\tilde{n}=1}^{\tilde{N}} e^{j2\pi x_{\tilde{n}}(\sin\theta - \sin\theta_0)}, \quad (8)$$

the meanings differs between them. (8) expresses the far-field strength in θ-direction when the beam is focused in θ_0-direction for phased array systems, while the AAF plays a main role in the overall performance of direction finding

systems. In (7), θ_j indicates a real DoA and θ_i indicates the estimated one, or θ_j can be the direction of the desired signal and θ_i the direction of the interfering signal. The angular regions of interest are Θ_J and Θ_I, respectively. The area formed by Θ_J and Θ_I is called the field-of-view (FoV), as shown in the black box in Fig. 1(a). It is worth mentioning that Θ_J and Θ_I are not necessarily the same. According to [18], the gain of an antenna does not decay sharply out of the angular field-of-view. And some factors, such as the multipath effect, can cause expansion of the interfering DoAs. In this paper, the range of real DoAs is considered to be larger than or equal to the range of estimated DoAs, i.e. $\Theta_J \subseteq \Theta_I$. Θ_I can be determined according to the radiation pattern of antenna elements and the multipath effect, and Θ_J can be determined according to the application scenario and the unambiguous requirement.

The $|AAF|$ takes values from 0 to 1. When $|AAF(\theta_i, \theta_j)| = 1$, the two directions θ_i and θ_j are completely indistinguishable, while the array can completely distinguish the two directions when $|AAF(\theta_i, \theta_j)| = 0$. The amplitude of the AAF is represented by a color map, and then the angular resolution and ambiguity-free region of the array can be seen clearly, as shown in Fig. 1(a).

The $|AAF|$ image is symmetric with respect to the oblique ridged main lobe, and takes its maximum value on it, i.e. $AAF(\theta_i, \theta_i) = 1$. As the distance between the two angles θ_i and θ_j near the main lobe increases, the correlation between the two steering vectors decreases gradually, and the ability of the array to distinguish targets in these two directions is also enhanced. Therefore, the main lobe width (MLW), such as -3dB MLW, can be used to evaluate the angular resolution of nonuniform arrays with equal aperture size. The region outside the main lobe is defined as the sidelobe region. The peak sidelobe level (SLL) in the FoV region determines whether angular ambiguity will appear in DoA estimations or not. In addition, SLL can also be used to evaluate the anti-interference ability of the array, the so-called dynamic range [2], to suppress clutter when estimating DoAs.

Fig. 1(a) also shows that the resolution of the array is related to the DoA. When the signal comes from the boresight direction $\theta = 0°$, the MLW is the narrowest, indicating that the highest angular resolution is achieved. As the DoA gradually deviates from the boresight direction, the MLW becomes wider, indicating that the angular resolution decreases. In (7), the nonlinearity of the sine function $\sin\theta$ results in this characteristic. To mitigate the impact of nonlinearity, we define the auxiliary variables

$$u_i = \sin\theta_i, \quad u_j = \sin\theta_j. \quad (9)$$

Then, the ambiguity function can be rewritten as the function of u_j and u_i,

$$AAF(u_i, u_j) = \frac{1}{MN} \sum_{m=1}^{M} \sum_{n=1}^{N} e^{j2\pi(t_m+r_n)(u_i-u_j)}. \quad (10)$$

The corresponding FoV interval is represented by Ω_J and Ω_I. A new AAF color map is shown in Fig. 1(b). It can be seen that the MLW is fixed, which means that the angular

resolution will not change with different DoAs measured by u_i and u_j. If the FoV of radar is set to $\Theta_J = [-\theta_{jmax}, \theta_{jmax}]$ and $\Theta_I = [-\theta_{imax}, \theta_{imax}]$, or $\Omega_J = [-u_{jmax}, u_{jmax}]$ and $\Omega_I = [-u_{imax}, u_{imax}]$, where $u_{jmax} = \sin\theta_{jmax}$ and $u_{imax} = \sin\theta_{imax}$, the dynamic range and resolution of the array can be evaluated with the SLL and MLW of the AAF in the region of $u_i \in \Omega_I$ and $u_j \in \Omega_J$.
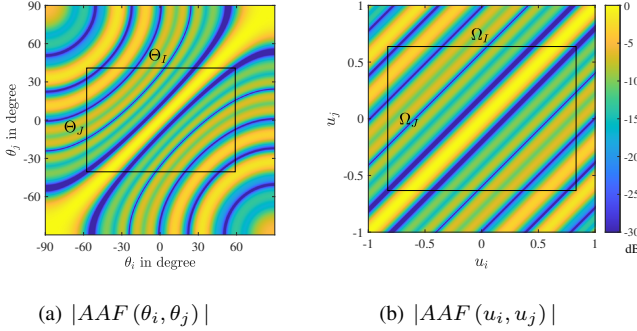

(a) $|AAF(\theta_i, \theta_j)|$ (b) $|AAF(u_i, u_j)|$

Fig. 1. The AAF of [17]; Θ_J, Θ_I, Ω_J and Ω_I are the regions of interest which form the FoV.

B. Expanded Beam Pattern (EBP)

The AAF pattern is evaluated using two variables u_i and u_j, which will increase computational complexity during optimization. Nevertheless, according to its symmetry property in Fig. 1(b), one can define an expanded beam pattern (EBP) as

$$f(u) = \frac{1}{MN} \sum_{m=1}^{M} \sum_{n=1}^{N} e^{j2\pi(t_m + r_n)u}, \qquad (11)$$

where

$$u = u_i - u_j \in [-u_{max}, u_{max}],$$
$$u_{max} = u_{jmax} + u_{imax} \qquad (12)$$

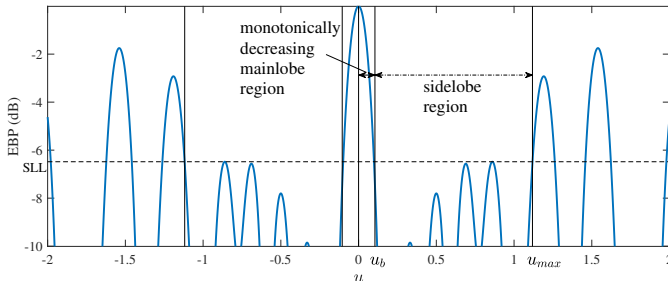Then (11) becomes a univariate function which contains all the information of AAF in the FoV.

Fig. 2. The EBP $|f(u)|$ of [17]; The SLL, u_b, and u_{max} are calculated by numerical methods, and they satisfy $f(u_b) = f(u_{max}) = $SLL, $f'(u_b) < 0$, $f'(u_{max}) > 0$.

Setting an appropriate variable $u_b = \sin\theta_b$, which represents the sidelobe starting point, one can define $[0, u_b]$ as a monotonically decreasing main lobe region as shown in Fig. 2. Then the normalized angular resolution can be assessed by

measuring half of the -3dB main lobe width (HMLW) of the EBP, which depends only on the array geometry. Furthermore, The sidelobe region is discretized into S uniform sampling points on the interval $[u_b, u_{max}]$, i.e.,

$$\Omega_S = \left\{ u_s \Big| u_s = u_b + \frac{s-1}{S-1}(u_{max} - u_b), \ s = 1, \cdots, S \right\}. \qquad (13)$$

C. Element Position Constraints

In practice, the antenna arrays are limited by aperture size. In order to mitigate the mutual coupling effect, a minimum array element spacing also needs to be considered. In terms of element position constraints of multistatic MIMO radar, we consider two common cases: In one case, the transmitting antenna and the receiving antenna are designed on the same dielectric substrate [16], and in another case, the transmitting antenna and the receiving antenna are designed on multiple dielectric substrates [8]. Since the EBP depends only on the relative position of the array elements rather than the absolute position [15], to reduce computational complexity, the position of the first transmitter or the first virtual element can be fixed in the algorithm. For two different cases, two types of constraints are given as follows:

1) Case 1: The transmitting and receiving antennas are on the same dielectric substrate. This means that their vertical coordinates are equal and their horizontal coordinates are not. In this case, the position of the first transmitting element is fixed, i.e.,

$$t_1 = 0,$$
$$\boldsymbol{d} = [0, t_2, \ldots, t_M, r_1, \ldots, r_N]^T. \qquad (14)$$

One can assume that all the receiving elements are located on the right side of the transmitting elements [16], that is, $r_n > t_m$. The constraints limit the minimum spacing between transmitting antennas Δt_m, the minimum spacing between receiving antennas Δr_n, the minimum spacing between transmitting antennas and receiving antennas Δd_{tr}, and the aperture size D. They can be written as

$$\text{s.t.} \quad t_m - t_{m-1} \geq \Delta t_m, \quad m = 2, \ldots, M,$$
$$r_n - r_{n-1} \geq \Delta r_n, \quad n = 2, \ldots, N,$$
$$r_1 - t_M \geq \Delta d_{tr},$$
$$r_N \leq D. \qquad (15)$$

If we define

$$\boldsymbol{C} = \begin{bmatrix} 1 & 0 & \cdots & \cdots & 0 \\ -1 & 1 & 0 & \cdots & 0 \\ 0 & -1 & 1 & 0\cdots & 0 \\ \vdots & & \ddots & \ddots & \\ 0 & \cdots & 0 & -1 & 1 \\ 0 & \cdots & \cdots & 0 & -1 \end{bmatrix}_{(M+N+1)\times(M+N)}$$

$$\boldsymbol{d}_c = [0, \Delta t_2, \cdots, \Delta t_M, \Delta d_{tr}, \Delta r_2, \cdots, \Delta r_N, -D]^T, \qquad (16)$$

(15) can be written in a matrix-vector form:

$$Cd - d_c \succeq 0. \tag{17}$$

2) Case 2: The transmitting antennas and the receiving antennas are distributed on two dielectric substrates, where their vertical coordinates are not equal and their horizontal coordinates can be equal. In this case, the positions of the first transmitting element and the first receiving element are fixed, i.e.,

$$t_1 = r_1 = 0$$
$$d = [0, t_2, \ldots, t_M, 0, r_2, \ldots, r_N]^T. \tag{18}$$

The position constraints limit Δt_m, Δr_n, the transmitting array aperture size D_t, and the receiving array aperture size D_r, and they can be written as

$$\begin{aligned} \text{s.t.} \quad & t_m - t_{m-1} \geq \Delta t_m, \quad m = 2, \ldots, M, \\ & r_n - r_{n-1} \geq \Delta r_n, \quad n = 2, \ldots, N, \\ & t_M \leq D_t, \\ & r_N \leq D_r. \end{aligned} \tag{19}$$

Define

$$\bar{C} = \begin{bmatrix} C_{(M+1) \times M} & 0 \\ 0 & C_{(N+1) \times N} \end{bmatrix},$$
$$\bar{d}_c = [0, \Delta t_2, \cdots, \Delta t_M, -D_t, 0, \Delta r_2, \cdots, \Delta r_N, -D_r]^T, \tag{20}$$

(19) can be written in a matrix-vector form:

$$\bar{C}d - \bar{d}_c \succeq 0. \tag{21}$$

Besides, for monostatic MIMO radar cases [38], other constraints can be added when $M = N$ such as

$$t_m = r_m + \Delta d_m \quad \text{or} \quad |t_m - r_m| \leq \Delta d_m \tag{22}$$

Due to space limitations, the monostatic case is not discussed in detail in this article.

D. Problem 1 Definition: SLL Optimization

We take the Case 1 constraint (17) as an example to establish the mathematical model for SLL optimization.

In the optimization of antenna position, d (e.g. t_m and r_n) is regarded as a variable of the EBP:

$$f(d, u) = \frac{1}{MN} \sum_{m=1}^{M} \sum_{n=1}^{N} e^{j2\pi(t_m + r_n)u}. \tag{23}$$

On the premise of keeping the angular resolution basically unchanged, it is desirable that there is no ambiguity in the FoV and that the dynamic range is as high as possible. The antenna positions need to be optimized so that the SLL of the given sidelobe region in the FoV can be as small as possible. We formulate the following minimax model with element position constraints:

$$\begin{aligned} \min_{d} \quad & \max_{u_s \in \Omega_s} \quad |f(d, u_s)| \\ \text{s.t.} \quad & Cd - d_c \succeq 0. \end{aligned} \tag{24}$$

E. Problem 2 Definition: MLW Optimization

The angular resolution is expected to be as high as possible without ambiguity in the FoV. Thus, we need to optimize the antenna positions so that the main lobe can be as narrow as possible while the SLL does not increase.

To describe the normalized angular resolution, we define an inverse function $u_{3dB} = |f|^{-1}(-3dB)$ as the -3dB HMLW when $|f(d, u)|$ decreases to -3dB in the main lobe region. Then, the formulation for optimizing the HMLW can be established as follows:

$$\begin{aligned} \min_{d} \quad & u_{3dB}(d) \\ \text{s.t.} \quad & |f_s(d)| \leq \epsilon, \quad s = 1, \cdots, S \\ & Cd - d_c \succeq 0 \end{aligned} \tag{25}$$

where ϵ is determined by the given SLL. Since $u_{3dB}(d)$ is the
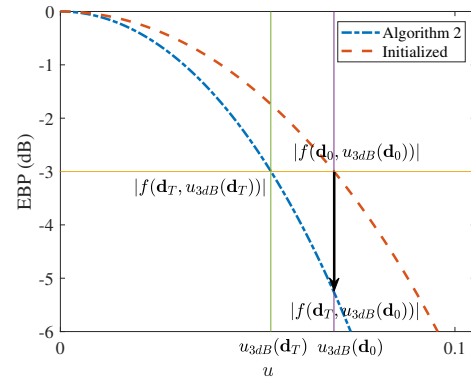
Fig. 3. Part of the EBP optimized via Algorithm 2.

inverse function of $|f(d, u)|$, its analytical expression cannot be obtained. To simplify the model, assume that the initial 3dB point is $u_{3dB}(d_0)$, which will be optimized via Algorithm 2 to be $u_{3dB}(d_T)$, as shown in Fig. 3. Obviously, the following inequality holds:

$$0 < u_{3dB}(d_T) \leq u_{3dB}(d_0) \leq u_b. \tag{26}$$

By choosing an appropriate u_b, it is reasonable to assume that the optimized pattern $|f(d_T, u)|$ is monotonically decreasing on the interval of $[0, u_b]$. Therefore, another inequality holds:

$$\begin{aligned} &|f(d_T, u_{3dB}(d_0))| \\ &< |f(d_T, u_{3dB}(d_T))| = |f(d_0, u_{3dB}(d_0))| = -3\text{dB}. \end{aligned} \tag{27}$$

If the -3dB HMLW becomes narrower, the function value $|f(d, u_{3dB}(d_0))|$ will also decrease after optimization. (26)-(27) prove that the optimization problem (25) with the objective function of $u_{3dB}(d)$ can be equivalently transformed into an optimization problem with the objective function of:

$$\begin{aligned} \min_{d} \quad & |f(d, u_c)|^2 \\ \text{s.t.} \quad & |f_s(d)|^2 \leq \epsilon^2, \quad s = 1, \cdots, S \\ & Cd - d_c \succeq 0, \end{aligned} \tag{28}$$

where $u_c \in (0, u_b)$ can be any point on the monotonically decreasing interval, such as $u_{3dB}(\boldsymbol{d}_0)$ or $u_{5dB}(\boldsymbol{d}_0)$. It should be noted that in addition to the objective function of (28), there may be other types of objective functions used to indirectly optimize the HMLW. For example, $\frac{\partial |f|^2}{\partial u}(\boldsymbol{d}, u_c)$ represents the slope of the pattern at u_c. If the optimized slope decreases, the HMLW will also decrease. For another example, $\int_0^{u_b} |f(\boldsymbol{d}, u)| \mathrm{d}u$ reflects the area of the main lobe region. If the area is reduced after optimization, the HMLW will also be reduced. Research on other objective functions will be carried out in our future work.

III. ALGORITHMS

In this section, we first propose two algorithms for solving Problem 1 and Problem 2, respectively. Then, a hybrid algorithm is developed for a trade-off between SLL and MLW.

A. Algorithm 1: SLL Optimization

To simplify the minimax objective function in (24), the auxiliary variable ε is defined as the upper bound of SLL, and $f(\boldsymbol{d}, u_s)$ is abbreviated to $f_s(\boldsymbol{d})$. Then, (24) can be rewritten as

$$\min_{\boldsymbol{d}, \varepsilon} \quad \gamma \varepsilon$$
$$\text{s.t.} \quad |f_s(\boldsymbol{d})| \leq \varepsilon, \quad s = 1, \ldots, S$$
$$\boldsymbol{C}\boldsymbol{d} - \boldsymbol{d}_c \succeq \boldsymbol{0} \tag{29}$$

where γ is the penalty factor of the objective function. When the order of magnitude difference between the objective function and the constraints is too large, the penalty factor is used to balance it. To separate the variables $\boldsymbol{d}$ and ε, the auxiliary variables y_s and the extra equality constraints are introduced, and (29) can be rewritten as

$$\min_{\boldsymbol{d}, \varepsilon, y_s} \quad \gamma \varepsilon$$
$$\text{s.t.} \quad y_s = f_s(\boldsymbol{d}), \quad s = 1, \ldots, S$$
$$|y_s| \leq \varepsilon, \quad s = 1, \ldots, S$$
$$\boldsymbol{C}\boldsymbol{d} - \boldsymbol{d}_c \succeq \boldsymbol{0}, \tag{30}$$

where $\boldsymbol{d}$ has been separated from the complex inequality constraints in (29). Our previous work [25]–[27] has demonstrated the distinct decomposition–coordination procedure and superior convergence property of ADMM. Therefore, we apply the ADMM to solve (30). According to [25], the augmented Lagrangian function with complex valued variables is constructed by

$$\mathcal{L}(\varepsilon, \boldsymbol{y}, \boldsymbol{d}, \boldsymbol{\lambda})$$
$$= \gamma \varepsilon + \sum_{s=1}^{S} \left(\Re[\lambda_s^*(y_s - f_s(\boldsymbol{d}))] + \frac{\rho}{2} |y_s - f_s(\boldsymbol{d})|^2 \right)$$
$$= \gamma \varepsilon + \frac{\rho}{2} \sum_{s=1}^{S} \left(|y_s - \bar{f}_s(\boldsymbol{d})|^2 - \left| \frac{\lambda_s}{\rho} \right|^2 \right), \tag{31}$$

where λ_s is a dual variable and $\rho > 0$ is a user-defined step size. Define $\bar{f}_s(\boldsymbol{d}) = f_s(\boldsymbol{d}) - \frac{\lambda_s}{\rho}$, $\boldsymbol{y} = [y_1, \cdots, y_S]^T$, $\boldsymbol{\lambda} = [\lambda_1, \cdots, \lambda_S]^T$, and $\boldsymbol{f}(\boldsymbol{d}) = [f_1(\boldsymbol{d}), \cdots, f_S(\boldsymbol{d})]^T$. Based on

ADMM [28], $\varepsilon, \boldsymbol{d}, \boldsymbol{y}$ and $\boldsymbol{\lambda}$ are determined by the following steps:

Step 1: $\{\varepsilon^{(t+1)}, \boldsymbol{y}^{(t+1)}\} := \arg\min_{\varepsilon, \boldsymbol{y}} \mathcal{L}(\varepsilon, \boldsymbol{y}, \boldsymbol{d}^{(t)}, \boldsymbol{\lambda}^{(t)})$
$$\text{s.t.} \quad |y_s| \leq \varepsilon, \quad s = 1, \ldots, S, \tag{32}$$

Step 2: $\boldsymbol{d}^{(t+1)} := \arg\min_{\boldsymbol{d}} \mathcal{L}(\varepsilon^{(t+1)}, \boldsymbol{y}^{(t+1)}, \boldsymbol{d}, \boldsymbol{\lambda}^{(t)})$
$$\text{s.t.} \quad \boldsymbol{C}\boldsymbol{d} - \boldsymbol{d}_c \succeq \boldsymbol{0}, \tag{33}$$

Step 3: $\boldsymbol{\lambda}^{(t+1)} := \boldsymbol{\lambda}^{(t)} + \rho \left(\boldsymbol{y}^{(t+1)} - \boldsymbol{f}(\boldsymbol{d}^{(t+1)}) \right), \tag{34}$

where t represents the number of iterations. Obviously, the complex optimization problem (30) has been divided into several simple subproblems by the above derivations (32)-(34). Among them, the subproblem (32) for updating ε and $\boldsymbol{y}$ and the subproblem (33) for updating $\boldsymbol{d}$ are only subject to inequality constraints, while (34) is the update rule for the dual variable $\boldsymbol{\lambda}$. Based on the aforementioned process, Algorithm 1 is described as follows, with details given in Appendix A.

Algorithm 1 SLL-Based Array Optimization Method

Input: initialized antenna positions $\boldsymbol{d}$, position constraints $\boldsymbol{d}_c$, FoV u_{max}, sidelobe starting point u_b, step size ρ, Lagrangian multiplier $\boldsymbol{\lambda}$, SLL upper bound ε_U, penalty factor γ, maximum number of iterations T, and stop tolerance η.
  while $t \leq T$ and $\max\{\alpha, \beta\} > \eta$ **do**
    $\varepsilon^{(t+1)}$ and $\boldsymbol{y}^{(t+1)}$ are determined by (45)-(51);
    $\boldsymbol{d}^{(t+1)}$ is determined by (52) via sequential quadratic programming (SQP);
    $\boldsymbol{\lambda}^{(t+1)}$ is determined by (34).
  end while
Output: optimal antenna positions $\boldsymbol{d}$ and optimal SLL ε.

B. Algorithm 2: MLW Optimization

To simplify the inequality constraints in (28), the auxiliary variable y_s and the auxiliary equality constraints are introduced. Abbreviating $f(\boldsymbol{d}, u_c)$ as $f_c(\boldsymbol{d})$, (28) can be rewritten as

$$\min_{\boldsymbol{d}, \boldsymbol{y}} \quad \gamma |f_c(\boldsymbol{d})|^2$$
$$\text{s.t.} \quad |f_s(\boldsymbol{d})|^2 - \epsilon^2 + y_s^2 = 0, \quad s = 1, \cdots, S$$
$$\boldsymbol{C}\boldsymbol{d} - \boldsymbol{d}_c \succeq 0, \tag{35}$$

where γ is the penalty factor of the objective function. When the order of magnitude difference between the objective function and the constraints is too large, the penalty factor is used to balance it. The optimization problem (35) can be solved based on the Lagrange multiplier method [39]. First, the augmented Lagrangian function is constructed as follows:

$$\mathcal{L}(\boldsymbol{y}, \boldsymbol{d}, \boldsymbol{\mu})$$
$$= \gamma |f_c(\boldsymbol{d})|^2 + \sum_{s=1}^{S} \left(-\mu_s[\tilde{f}_s(\boldsymbol{d}) + y_s^2] + \frac{\rho}{2}[\tilde{f}_s(\boldsymbol{d}) + y_s^2]^2 \right), \tag{36}$$

where μ_s is a dual variable, and $\rho > 0$ is a user-defined step size. Define $\boldsymbol{y} = [y_1, \cdots, y_S]^T$, $\boldsymbol{\mu} = [\mu_1, \cdots, \mu_S]^T$, $\tilde{f}_s(\boldsymbol{d}) = |f_s(\boldsymbol{d})|^2 - \epsilon^2$, and $\tilde{\boldsymbol{f}}(\boldsymbol{d}) = [\tilde{f}_1(\boldsymbol{d}), \cdots, \tilde{f}_S(\boldsymbol{d})]^T$. In order to eliminate y_s, by $\nabla_{\boldsymbol{y}} \mathcal{L}(\boldsymbol{y}, \boldsymbol{d}, \boldsymbol{\mu}) = \boldsymbol{0}$, we have

$$y_s[\rho \boldsymbol{y}_s^2 - (\mu_s - \rho \tilde{f}_s(\boldsymbol{d}))] = 0, \quad s = 1, \cdots, S. \quad (37)$$

As a result, y_s can be expressed as a function of $\boldsymbol{d}$.

$$y_s^2 = \begin{cases} \frac{1}{\rho}[\mu_s - \rho \tilde{f}_s(\boldsymbol{d})] & \text{if } \mu_s - \rho \tilde{f}_s(\boldsymbol{d}) > 0 \\ 0 & \text{otherwise} \end{cases}$$
$$\text{for } s = 1, \cdots, S. \quad (38)$$

Substitute it into (36) to eliminate $\boldsymbol{y}$, and then we have

$$\mathcal{L}(\boldsymbol{d}, \boldsymbol{\mu}) = \min_{\boldsymbol{y}} \mathcal{L}(\boldsymbol{y}, \boldsymbol{d}, \boldsymbol{\mu})$$
$$= \gamma |f_c(\boldsymbol{d})|^2 + \sum_{s=1}^S \frac{1}{2\rho}[(\min\{0, \mu_s - \rho \tilde{f}_s(\boldsymbol{d})\})^2 - \mu_s^2]. \quad (39)$$

By substituting (38) into the multiplier update rule $\mu_s^{(t+1)} = \mu_s^{(t)} - \rho(\tilde{f}_s(\boldsymbol{d}) + y_s^2)$, we obtain

$$\mu_s^{(t+1)} = \begin{cases} 0 & \text{if } \mu_s^{(t)} - \rho \tilde{f}_s(\boldsymbol{d}) > 0 \\ \mu_s^{(t)} - \rho \tilde{f}_s(\boldsymbol{d}) & \text{otherwise} \end{cases}$$
$$\text{for } s = 1, \cdots, S. \quad (40)$$

Similarly, the stopping criterion can be obtained by substituting (38) into $|\tilde{f}_s(\boldsymbol{d}) + y_s^2| \leq \eta$:

$$|\max\{\tilde{f}_s(\boldsymbol{d}), \frac{\mu_s^{(t)}}{\rho}\}| \leq \eta, \quad s = 1, \cdots, S. \quad (41)$$

Based on the Lagrange multiplier method, the variables $\boldsymbol{d}$ and $\boldsymbol{\mu}$ are determined by the following update rules:

Step 1:

$$\boldsymbol{d}^{(t+1)} := \arg\min_{\boldsymbol{d}} \mathcal{L}(\boldsymbol{d}, \boldsymbol{\mu}^{(t)})$$
$$\text{s.t. } \boldsymbol{C}\boldsymbol{d} - \boldsymbol{d}_c \succeq \boldsymbol{0} \quad (42)$$

To determine $\boldsymbol{d}^{(t+1)}$, the subproblem (42) is derived with given $\boldsymbol{\mu}^{(t)}$. The constant terms in (39) can be ignored, and we have

$$\min_{\boldsymbol{d}} \quad \gamma |f_c(\boldsymbol{d})|^2 + \frac{1}{2\rho} \sum_{s=1}^S (\min\{0, \mu_s - \rho \tilde{f}_s(\boldsymbol{d})\})^2$$
$$\Rightarrow \min_{\boldsymbol{d}} \quad F_2(\boldsymbol{d})$$
$$\text{s.t. } \boldsymbol{C}\boldsymbol{d} - \boldsymbol{d}_c \succeq \boldsymbol{0} \quad (43)$$

Because the constraints are linear inequalities, sequential quadratic programming (SQP) [39] can be used to solve (43) with fast convergence, high computational efficiency, and strong boundary search ability. The derivation of $\nabla_{\boldsymbol{d}} \boldsymbol{F}_2$ is given in Appendix B.

Next, with given $\boldsymbol{d}^{(t+1)}$, the Lagrangian multiplier $\boldsymbol{\mu}$ is updated by

Step 2:

$$\mu_s^{(t+1)} := \min\{0, \mu_s^{(t)} - \rho \tilde{f}_s(\boldsymbol{d})\}, \quad s = 1, \cdots, S \quad (44)$$

Repeat steps 1-2 until $t > T$ (T is the maximum number of iterations) or the stop criterion (41) is met.

Algorithm 2 MLW-Based Array Optimization Method

Input: initialized antenna positions $\boldsymbol{d}$, position constraints $\boldsymbol{d}_c$, FoV u_{max}, sidelobe starting point u_b, a point u_c on the monotonically decreasing interval, step size ρ, Lagrangian multiplier $\boldsymbol{\mu}$, SLL ϵ, penalty factor γ, maximum number of iterations T, and stop tolerance η.
  while (41) does not hold and $t \leq T$ **do**
    $\boldsymbol{d}^{(t+1)}$ is determined by (43) via SQP;
    $\boldsymbol{\mu}^{(t+1)}$ is determined by (44).
  end while
Output: optimal antenna positions $\boldsymbol{d}$, optimized SLL ε, optimized -3dB point u_c and sidelobe starting point u_b.

Based on the aforementioned discussions, the method is summarized as follows:

Algorithm 1 and Algorithm 2 apply to different scenarios. The first is used in the scenario where the power and orientation information of interference are unclear, such as in the mine scene of autonomous driving. In this case, the ambiguity function needs to have a lower SLL to suppress potential strong interference. Algorithm 2 is more suitable for static scenarios, such as indoor radar, where the information of interference is usually known. In order to have a higher angular resolution, a narrower MLW becomes more attractive. Generally speaking, there is a parametric trade-off between MLW and SLL [22], and we expect most of the results to lie on the SLL-MLW Pareto front boundary [24], which is the state at which resources in a given system are optimized in a way that one dimension cannot improve without the second worsening [40]. Moreover, Algorithm 1 and Algorithm 2 have difficulties in parameter selection. If the set sidelobe region in Algorithm 1 is too large, that is, u_b is too small, the optimized SLL tends to be very high; If the SLL ϵ set in Algorithm 2 is too small, the optimization problem (28) may be infeasible. Therefore, it is necessary to develop an algorithm that does not require too much parameter tuning.

[34] proposes a modified real genetic algorithm (MGA) for sparse linear array synthesis with multiple constraints. Similarly, MGA can also be used to optimize the MIMO array geometry described in this paper. We propose a three-step hybrid algorithm to solve the SLL and MLW optimization problem without a pre-given mask [41], and the specific steps are shown in Algorithm 3.

Initial values of variables often have a great influence on the results of non-convex and nonlinear optimization problems. Considering the low efficiency of the commonly used random initialization, we first use MGA to obtain some good initial solutions and then calculate the exact solution iteratively based on Algorithm 1 and Algorithm 2. This hybrid algorithm benefits from the global optimization capability of heuristic algorithms and the accuracy of numerical optimization algorithms.

IV. SIMULATION RESULTS

To demonstrate the performance of the proposed methods, simulations are performed to evaluate the properties of the optimized sparse arrays.

Algorithm 3 Hybrid Algorithm for Pareto Optimality

Input: number of transmitting antennas M and receiving antennas N, position constraints $\boldsymbol{d}_c$, FoV u_{max}, step size ρ_1 for Algorithm 1, ρ_2 for Algorithm 2, Lagrangian multiplier $\boldsymbol{\lambda}$ for Algorithm 1, $\boldsymbol{\mu}$ for Algorithm 2, maximum number of iterations T, stop tolerance η, population size, crossover rate, mutation rate, and maximum generations of MGA.

1: **Step 1:** According to MGA [34], the initialized antenna positions $\boldsymbol{d}$ are synthesized to achieve a minimum SLL ε.

2: **while** $\varepsilon^{(i)} \leq \varepsilon^{(i-1)}$ and $u_b^{(i)} \leq u_b^{(i-1)}$ and $u_c^{(i)} \leq u_c^{(i-1)}$ **do**

3:     The dichotomy method is used to search for the sidelobe starting point u_b and the -3dB point u_c on the monotone decreasing interval.

4:     **Step 2:** $\varepsilon_U \leftarrow \varepsilon$, optimize $\boldsymbol{d}$ via Algorithm 1, and update the optimized SLL ε.

5:     **Step 3:** $\epsilon \leftarrow \varepsilon$, optimize $\boldsymbol{d}$ via Algorithm 2, and update the optimized SLL ε.

6:     $i = i + 1$.

7: **end while**

8: The dichotomy method is used to search for the sidelobe starting point u_b and the -3dB point u_c on the monotone decreasing interval. The variables $\varepsilon^{(i)}, u_b^{(i)}, u_c^{(i)}$ are saved.

Output: optimal antenna positions $\boldsymbol{d}$, optimized SLL ε, optimized -3dB point u_c and sidelobe starting point u_b.

A. Numerical simulation 1 with 2T3R configuration

In the case of fewer antennas, to reduce the cost, the transmitting and receiving antennas are usually placed on the same dielectric substrate. [16] and [17] have used GA to optimize positions of MIMO array elements. Under the constraints of a certain SLL, aperture size and element spacing, they try to maximize the ambiguity-free region, which is also defined as u_{max} in (12). Due to the different objective functions of Algorithm 1 (A1), Algorithm 2 (A2) and GA [17], it is difficult for a fair comparison. Moreover, when the number of antennas is very small, e.g., 2T3R and 4T4R configurations, there are only a few variables with so many constraints, resulting in a very low degree of freedom for optimization, so that the results of most algorithms can approach their respective pareto optimality. Therefore, we can only observe small differences in the overall performance of each algorithm, so as to see which parameter it sacrifices at the expense of improving its objective function.

The parameters in this experiment are consistent with [16]. The aperture size and minimum element spacing are $D = 14.13$ and $\Delta t_m = \Delta r_n = \Delta d_{tr} = 1.17$. As shown in Fig. 2, the initialized parameters of A1 and A2: SLL, u_b, u_{max} and u_c can be calculated by numerical methods from the results in [16], where u_{max} is also consistent with the conventional MIMO array with 0.8 wavelength virtual element spacing (0.8 uniform). The maximum number of iterations for both algorithms is set to $T = 1000$, and the stop residuals are $\eta = 10^{-6}$.

We use the MGA to generate 1000 initialized antenna positions, and then use A1 and A2 to optimize each solution

TABLE I
SIMULATION 1: 2T3R RESULTS

Array	Antenna Positions $\boldsymbol{d}$	SLL	HMLW	u_{max}
A1	$[0, 2.46, 4.80, 6.61, 8.06]^T$	-7.02dB	0.071	1.136
A2	$[0, 3.42, 4.80, 7.41, 8.93]^T$	-6.35dB	0.053	1.118
GA [16]	$[0, 2.54, 4.80, 6.68, 8.12]^T$	-6.48dB	0.069	1.118
0.8 uniform	$[0, 2.4, 4.8, 5.6, 6.4]^T$	-12.43dB	0.093	1.118

obtained by MGA. Finally, we select the optimal solution minimizing the objective function. The antenna positions of the four arrays are shown in Fig. 4. The EBPs synthesized by the four arrays are shown in Fig. 5. Table I gives the antenna positions, SLLs, -3dB HMLW and FoV u_{max} of the four arrays. Compared with the pattern synthesized by GA [16], results obtained by the proposed A1 and A2 have their respective properties.

A1 achieves a lower SLL, a larger u_{max}, and a smaller aperture size with a small sacrifice in HMLW. By comparing the antenna position difference between A1 and GA, it can be seen that A1 actually provides a fine-tuning of the result of GA. If we follow the criterion of [16], i.e., without considering HMLW, our proposed method has a higher accuracy.

A2 achieves a much narrower HMLW at the cost of aperture size and SLL. Due to the strong correlation between the beam width and the second moment about the mean of the array element positions [32], Algorithm 2 utilizes a larger available aperture, but the result still satisfies the pre-set maximum aperture constraint. According to [30], a small MLW is more important for DOA estimation than a low SLL and hence the sacrifice of A2 is justifiable.
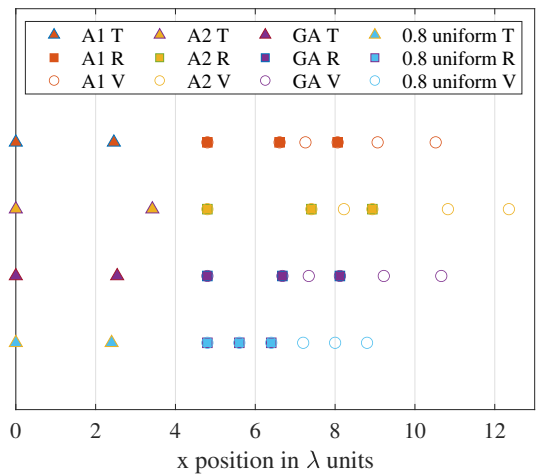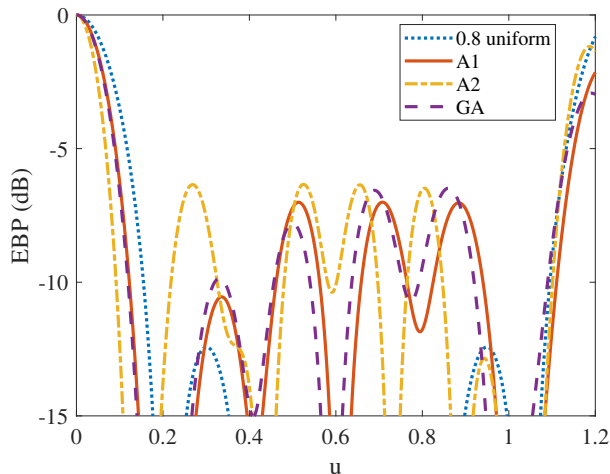

Fig. 4. Simulation 1: 2T3R antenna positions of Algorithm 1 (A1), Algorithm 2 (A2), GA [16], and conventional MIMO array with 0.8 wavelength virtual element spacing (0.8 uniform), where T, R, and V denote transmitter, receiver, and virtual array element, respectively.

B. Full wave simulation with the 2T3R result of A2

The numerical 2T3R result of A2 is implemented in a full-wave solver (ANSYS HFSS). For this purpose, the microstrip patch antenna array is designed on a substrate (Rogers

Fig. 5. Simulation 1: EBPs $|f(u)|$ of 2T3R arrays.

(a) Numerical result   (b) Full-wave result

Fig. 7. The AAF comparison between numerical result and full-wave result.

RO3003) with nominal permittivity $\varepsilon_r = 3$ as shown in Fig. 6. Each MIMO element employs an eight-element standing-wave series-fed antenna array [42] with Dolph–Chebyshev current distribution, which is matched in the range of 77-79 GHz.

The mutual coupling between their elements can be accounted for by considering the radiation pattern of each antenna element as mentioned in (2). These patterns obtained by HFSS simulations deviate from the average element pattern assumed in (3) for the numerical examples. To include the effects of mutual coupling, the AAF calculated by the radiation patterns of all the elements obtained by the HFSS simulations are shown in Fig. 7(b). For comparison, the numerical result is presented in Fig. 7(a). Obviously, the two AAF images are almost the same, which indicates that the numerical AAF derived by average element pattern takes into account the effect of mutual coupling and thus can approximate the real AAF very well.
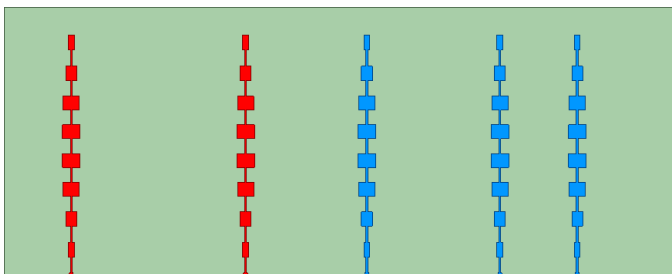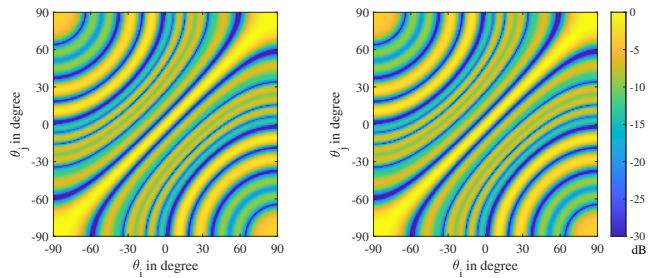

Fig. 6. Full wave simulation: The model of 2T3R MIMO antennas.

C. Numerical simulation 2 with 4T4R configuration

In the case of the 4T4R configuration, the transmitting antennas and the receiving antennas are considered to be placed on two dielectric substrates. Recently, [43] proposed a hybrid approach for SLL and MLW reduction to numerically determine an optimal 4T4R MIMO array considering simulated annealing and particle swarm optimization (SA-PSO). In this experiment, we evaluate the performance of Algorithm 3 (A3)

TABLE II
SIMULATION 3: 4T4R RESULTS

Array	Antenna Positions $\boldsymbol{d}$	SLL	HMLW
A3	[0, 1.69, 3.56, 5.25, 0, 0.92, 2.03, 2.92]^T	-19.44dB	0.057
SA-PSO [43]	[0, 1.64, 3.53, 5.08, 0, 0.88, 1.86, 2.71]^T	-18.78dB	0.059
0.5 uniform	[0, 2, 4, 6, 0, 0.5, 1.0, 1.5]^T	-13.15dB	0.055

and compare it with SA-PSO and conventional MIMO array with half-wavelength virtual element spacing (0.5 uniform). The aperture size and minimum element spacing are set to $D_t = 7.5$, $D_r = 7.5$ and $\Delta t_m = \Delta r_n = 0.15$. $u_{max} = 1$ is calculated by numerical methods from the results in [43]. Table II and Fig. 9 show that both the SLL and HMLW of the array designed by Algorithm 3 are better than those of the SA-PSO approach at the cost of a slightly larger aperture, which still satisfies the aperture size constraints and is therefore acceptable.
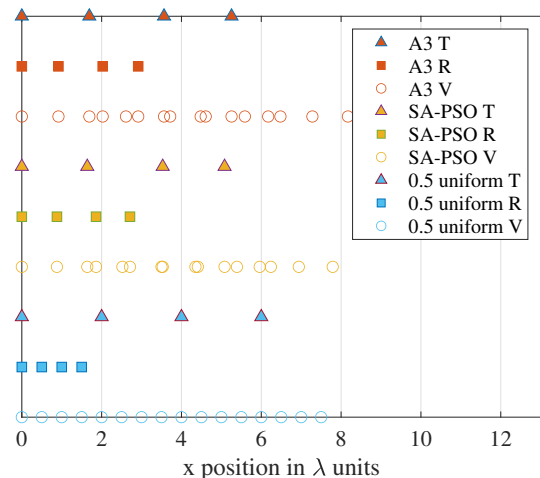

Fig. 8. Simulation 2: 4T4R antenna positions of Algorithm 3 (A3), SA-PSO [43], and conventional MIMO array with 0.5 wavelength virtual element spacing (0.5 uniform), where T, R, and V denote transmitter, receiver, and virtual array element, respectively.
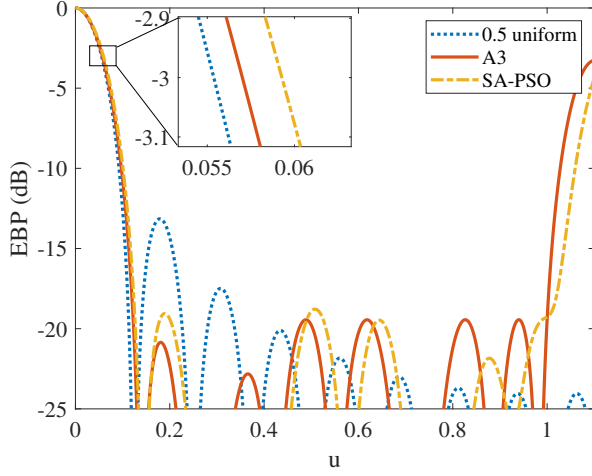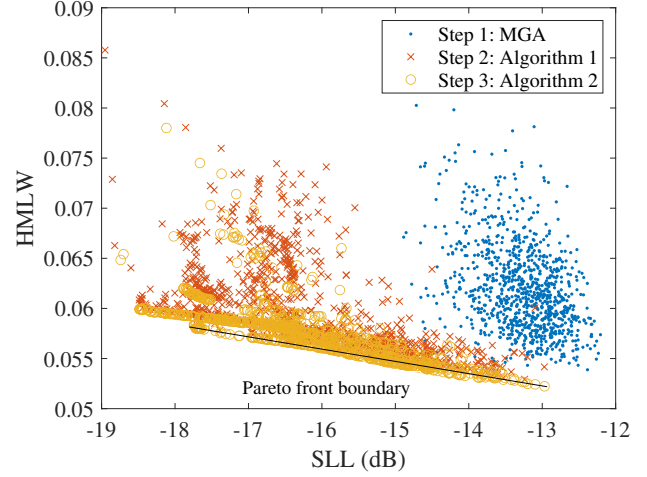
Fig. 9. Simulation 2: EBPs $|f(u)|$ of 4T4R arrays.

TABLE III
SIMULATION 3: 1T16R ANTENNA POSITIONS, SLLS, AND HMLWS WITH $\theta_j = -70°$

Array	Receiver Positions	SLL	HMLW
ULA	$[0, 0.5, 1, 1.5,$ $2, 2.5, 3, 3.5,$ $4, 4.5, 5, 5.5,$ $6, 6.5, 7, 7.5]^T$	-13.15dB	0.055
Pareto -17.7dB	$[0, 0.6224, 1.0222, 1.5587,$ $2.0444, 2.5283, 2.9740, 3.4130,$ $3.8366, 4.2653, 4.6769, 5.1379,$ $5.6209, 6.1137, 7.1143, 7.5]^T$	-17.70dB	0.058
Pareto -13.2dB	$[0, 0.2734, 0.8006, 1.5143,$ $1.8076, 2.4649, 2.9678, 3.4002,$ $3.9951, 4.3865, 5.0222, 5.4188,$ $6.2469, 7.0069, 7.3500, 7.5]^T$	-13.20dB	0.052

D. Numerical simulation 3 with 1T16R configuration

In this experiment, a 1T16R configuration is employed to evaluate sparse and uniform arrays with equal aperture size and equal number of antennas. The aperture size and minimum element spacing are set to $D_r = 7.5$, $\Delta r_n = 0.15$. The 1T16R array is optimized 1000 times using A3, and then the results of SLL and HMLW are plotted in Fig. 10. The SLLs are significantly reduced by A1 in the hybrid optimization process, and A2 further reduces the HMLWs. It is noticed that most of the results of Step 3 lie on the SLL-HMLW Pareto front boundary [24]. The proposed method can make almost every solution converge to this boundary. However, it is very difficult to reach the boundary for heuristic algorithms without significantly increased iterations.

Two results with an SLL of -13.2dB and -17.7dB are selected from this boundary, and their antenna positions and EBPs are shown in Figs. 11 and 12, respectively. Fig. 12 and Table III demonstrate that the MLW of Pareto -13.2dB is narrower than that of the uniform linear array (ULA), and the SLL is not higher than that of the ULA. On the other hand, Pareto -17.7dB can achieve a lower SLL at the cost of MLW.

Fig. 10. Simulation 3: Optimize 1T16R arrays 1000 times using Algorithm 3
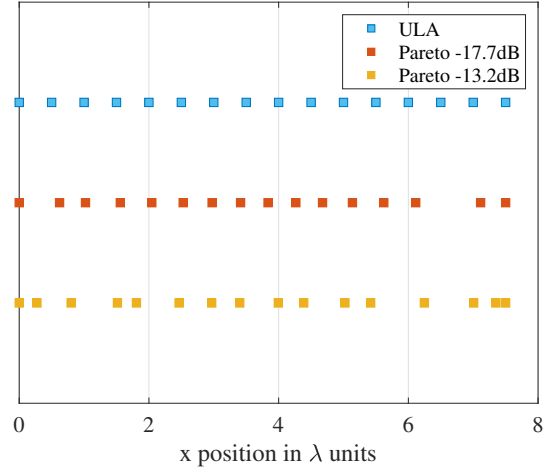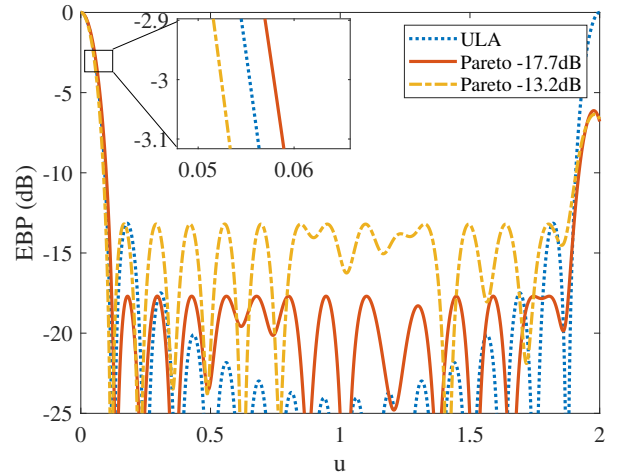

Fig. 11. Simulation 3: 1T16R receiver positions of A3 on the Pareto front boundary and ULA with 0.5 wavelength element spacing

Fig. 12. Simulation 3: EBPs $|f(u)|$ of 1T16R arrays.

E. Numerical simulation 4: DoA Estimation

To compare the DoA estimation performance of the three arrays in Table III, we use the Capon method [44] to estimate the spatial spectra corresponding to the three 1T16R arrays, as shown in Figs. 13 and 14. Two targets with equal receiving power are assumed to be located at $-70°$ and $-58°$. In Fig. 13, the SNR is set to -7dB. The spectra show that only the sparse array optimized via A3 with a -13.2dB SLL can distinguish the two close targets, which illustrates that a narrower MLW can achieve a higher angular resolution. To our best knowledge, this is the first time to show that the angular resolution of sparse arrays with equal aperture size may exceed that of uniform arrays when common DoA estimation methods are employed, such as DBF, Capon, MUSIC, OMP, IAA, etc [2]. However, the cost is that the noise floor of the spatial spectrum increases, i.e., the dynamic range decreases, which is consistent with the sidelobe performance in Fig. 12. At a higher SNR of 3dB, as shown in Fig. 14, the effect of sidelobe on the noise floor is reduced, and the narrower MLW makes the spectral peaks at the target locations sharper, which means that the narrower MLW also achieves a higher angular accuracy.
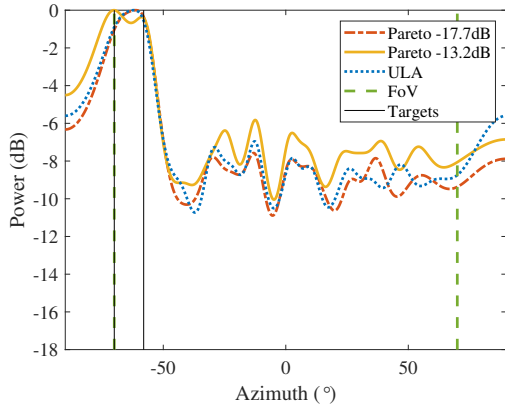

Fig. 13. Angle finding via Capon using the three arrays mentioned in Table III. The SNR is set to -7 dB.
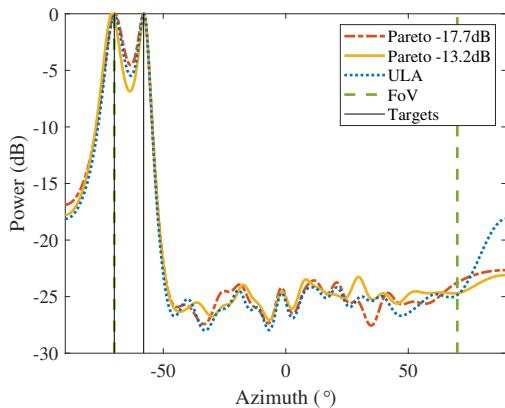

Fig. 14. Angle finding via Capon using the three arrays mentioned in Table III. The SNR is set to 3 dB.

V. CONCLUSIONS

In this article, a new approach for super-resolution and ambiguity-free sparse array geometry optimization in MIMO radar has been proposed. The properties of the angular ambiguity function are analyzed and the problem can be simplified into a EBP synthesis model. To obtain the optimal SLL, MLW and Pareto front boundary, several different problems with aperture size and element spacing constraints are formulated and algorithms for handling different objective functions are developed. Their performances have been investigated through numerical and full wave simulations, which show that the proposed methods can effectively improve the performance of DoA estimation for sparse arrays.

It is worth noting that although the concepts in this paper are developed for MIMO radars, due to high similarity of the mathematical models, the modeling and algorithms presented in this paper can also be extended to pencil beam pattern synthesis for sparse phased arrays such as [37], which is a more familiar problem in the field of antennas and propagation.

APPENDIX A
ALGORITHM 1

First, the subproblem (32) is derived with given $\boldsymbol{d}^{(t)}$ and $\boldsymbol{\lambda}^{(t)}$ to determine $\varepsilon^{(t+1)}$ and $\boldsymbol{y}^{(t+1)}$.

The constant terms in (31) can be ignored when $\boldsymbol{d}^{(t)}$ and $\boldsymbol{\lambda}^{(t)}$ are given, and we have

$$\min_{\varepsilon, y_s} \quad \gamma\varepsilon + \frac{\rho}{2}\sum_{s=1}^{S}|y_s - \bar{f}_s|^2$$
$$\text{s.t.} \quad |y_s| \le \varepsilon, \quad s = 1, \cdots, S. \tag{45}$$

When ε is provided, the optimal y_s is given by

$$y_s = \begin{cases} \varepsilon \times \exp(j\angle\bar{f}_s) & \text{if } |\bar{f}_s| \ge \varepsilon \\ \bar{f}_s & \text{if } |\bar{f}_s| < \varepsilon \end{cases}$$
$$\text{for } s = 1, \cdots, S. \tag{46}$$

Substituting (46) into (45), (45) is converted into an optimization problem with a single variable ε:

$$\min_{\varepsilon} \quad \gamma\varepsilon + \frac{\rho}{2}\sum_{s=1}^{S}U_s(\varepsilon)\left(\varepsilon - |\bar{f}_s|\right)^2$$
$$\text{s.t.} \quad \varepsilon \in [\varepsilon_L, \varepsilon_U], \tag{47}$$

where the region $\varepsilon \in [\varepsilon_L, \varepsilon_U]$ is the prior information of ε. It is easy to see that the objective functions in (46) and (47) are piecewise functions that depend on the value of the unit-step functions as follows:

$$U_s(\varepsilon) = \begin{cases} 1 & \text{if } |\bar{f}_s| \ge \varepsilon \\ 0 & \text{if } |\bar{f}_s| < \varepsilon \end{cases}$$
$$\text{for } s = 1, \cdots, S. \tag{48}$$

To solve (47), $\varepsilon = |\bar{f}_s|$ for $s = 1, \cdots, S$ are selected as reasonable turning points on the interval $[\varepsilon_L, \varepsilon_U]$. These S turning points are listed in ascending order and marked as $\{\varepsilon_1^{(t+1)}, \cdots, \varepsilon_K^{(t+1)}\}$, where $K \le S$. Thus, the interval $[\varepsilon_L, \varepsilon_U]$ can be divided into $K + 1$ sub-intervals

$[\varepsilon_L, \varepsilon_1^{(t+1)}), [\varepsilon_1^{(t+1)}, \varepsilon_2^{(t+1)}), \ldots, [\varepsilon_K^{(t+1)}, \varepsilon_U]$. On each sub-interval, the step functions $U_s(\varepsilon)$ for $s = 1, \cdots, S$ have specific values. As a result, (47) has different expressions on different sub-intervals. For example, for the k-th sub-interval $\varepsilon \in [\varepsilon_{k-1}^{(t+1)}, \varepsilon_k^{(t+1)}]$, (47) can be rewritten as

$$\min_{\varepsilon} \quad A_k \varepsilon^2 + B_k \varepsilon + C_k$$
$$\text{s.t.} \quad \varepsilon \in [\varepsilon_{k-1}^{(t+1)}, \varepsilon_k^{(t+1)}], \tag{49}$$

where

$$A_k = \frac{\rho}{2} \sum_{s=1}^{S} U_s(\varepsilon), \quad B_k = \gamma - \rho \sum_{s=1}^{S} U_s(\varepsilon) \left| \bar{f}_s \right|,$$
$$C_k = \frac{\rho}{2} \sum_{s=1}^{S} U_s(\varepsilon) \left| \bar{f}_s \right|^2. \tag{50}$$

Therefore, for the k-th sub-interval $\varepsilon \in [\varepsilon_{k-1}^{(t+1)}, \varepsilon_k^{(t+1)}]$, the optimal variable $\hat{\varepsilon}_k$ can be obtained easily by finding the minimum of the quadratic function, and the corresponding minimum of $A_k \varepsilon^2 + B_k \varepsilon + C_k$ is denoted as Q_k. By selecting the smallest one from all the $K + 1$ minimal values for the $K + 1$ sub-intervals, such as $Q_i = \min\{Q_1, \ldots, Q_{K+1}\}$, we determine $\varepsilon^{(t+1)}$ as

$$\varepsilon^{(t+1)} = \hat{\varepsilon}_i, \tag{51}$$

where $\hat{\varepsilon}_i$ is the extreme point corresponding to Q_i. Once $\varepsilon^{(t+1)}$ is obtained, $y_s^{(t+1)}$ can be derived by (46).

Next, the subproblem (33) is derived with given $\varepsilon^{(t+1)}, \boldsymbol{y}^{(t+1)}$ and $\boldsymbol{\lambda}^{(t)}$ to determine $\boldsymbol{d}^{(t+1)}$.

The constant terms in (31) can be ignored, and we have

$$\min_{\boldsymbol{d}} \quad \frac{\rho}{2} \sum_{s=1}^{S} \left| y_s - f_s(\boldsymbol{d}) + \frac{\lambda_s}{\rho} \right|^2$$
$$\Rightarrow \min_{\boldsymbol{d}} \quad F(\boldsymbol{d})$$
$$\text{s.t.} \quad \boldsymbol{Cd} - \boldsymbol{d}_c \succeq \boldsymbol{0}. \tag{52}$$

This is a nonlinear optimization problem with linear inequality constraints. Sequential quadratic programming (SQP) [39] is one of the most effective methods for solving constrained nonlinear optimization problems given its fast convergence, high computational efficiency, and strong boundary search ability. Thus, SQP is used to solve (52). Define $\nabla_{\boldsymbol{d}} F$ as the gradient of $F(\boldsymbol{d})$ which is derived in Appendix B.

Then, the Lagrangian multiplier $\boldsymbol{\lambda}^{(t+1)}$ is updated with given $\varepsilon^{(t+1)}, \boldsymbol{y}^{(t+1)}$ and $\boldsymbol{d}^{(t+1)}$ as shown by (34).

Finally, according to the ADMM stopping criterion given by [45], if

$$\max\{\alpha, \beta\} \leq \eta$$
$$\text{where}$$
$$\alpha = \left\| \boldsymbol{f}(\boldsymbol{d}^{(t+1)}) - \boldsymbol{f}(\boldsymbol{d}^{(t)}) \right\|_{\infty}$$
$$= \max_s \left| f_s(\boldsymbol{d}^{(t+1)}) - f_s(\boldsymbol{d}^{(t)}) \right|$$
$$\beta = \left\| \boldsymbol{y}^{(t+1)} - \boldsymbol{f}(\boldsymbol{d}^{(t+1)}) \right\|, \tag{53}$$

or $t > T$ (T is the maximum number of iterations), the calculation will stop. Otherwise, set $t := t + 1$, and go to **Step 1**.

APPENDIX B
ON COMPUTATION OF $\nabla_{\boldsymbol{d}} F$ AND $\nabla_{\boldsymbol{d}} F_2$

In (52), the gradient of objective function is given by

$$\nabla_{\boldsymbol{d}} F = \frac{\rho}{2} \sum_{s=1}^{S} \left((-\nabla_{\boldsymbol{d}} f_s)(y_s^* - f_s^*(\boldsymbol{d}) + \frac{\lambda_s^*}{\rho}) \right.$$
$$\left. + (y_s - f_s(\boldsymbol{d}) + \frac{\lambda_s}{\rho})(-\nabla_{\boldsymbol{d}} f_s^*) \right)$$
$$= \frac{\rho}{2} \sum_{s=1}^{S} \left((-\nabla_{\boldsymbol{d}} f_s)(y_s^* - f_s^*(\boldsymbol{d}) + \frac{\lambda_s^*}{\rho}) \right.$$
$$\left. + (y_s - f_s(\boldsymbol{d}) + \frac{\lambda_s}{\rho})(-\nabla_{\boldsymbol{d}} f_s)^* \right), \tag{54}$$

For different types of element position constraints, $\nabla_{\boldsymbol{d}} f_s$ has different forms.

1) Case 1:

$$\nabla_{\boldsymbol{d}} f_s = \begin{bmatrix} 0 & \frac{\partial f_s}{\partial t_2} & \cdots & \frac{\partial f_s}{\partial t_M} & \frac{\partial f_s}{\partial r_1} & \cdots & \frac{\partial f_s}{\partial r_N} \end{bmatrix}^T, \tag{55}$$

2) Case 2:

$$\nabla_{\boldsymbol{d}} f_s = \begin{bmatrix} 0 & \frac{\partial f_s}{\partial t_2} & \cdots & \frac{\partial f_s}{\partial t_M} & 0 & \frac{\partial f_s}{\partial r_2} & \cdots & \frac{\partial f_s}{\partial r_N} \end{bmatrix}^T, \tag{56}$$

where

$$\frac{\partial f_s}{\partial t_m} = \frac{1}{MN} \sum_{n=1}^{N} j2\pi u_s e^{j2\pi(t_m + r_n)u_s}, \tag{57}$$

$$\frac{\partial f_s}{\partial r_n} = \frac{1}{MN} \sum_{m=1}^{M} j2\pi u_s e^{j2\pi(t_m + r_n)u_s}. \tag{58}$$

To simplify $F_2(\boldsymbol{d})$ and $\nabla_{\boldsymbol{d}} F_2$ in Step 1 of Algorithm 2, we define step functions as

$$V_s = \begin{cases} 0 & \text{if } \lambda_s - \rho \tilde{f}_s(\boldsymbol{d}) > 0 \\ 1 & \text{otherwise} \end{cases}$$
$$\text{for } s = 1, \cdots, S. \tag{59}$$

Then, the piecewise function in (43) can be written in the form of the step function

$$F_2(\boldsymbol{d}) = \alpha |f_c(\boldsymbol{d})|^2 + \frac{1}{2\rho} \sum_{s=1}^{S} V_s (\lambda_s - \rho \tilde{f}_s(\boldsymbol{d}))^2. \tag{60}$$

$$\nabla_{\boldsymbol{d}} F_2 = \alpha \nabla_{\boldsymbol{d}} |f_c|^2 + \frac{1}{\rho} \sum_{s=1}^{S} V_s (\lambda_s - \rho \tilde{f}_s(\boldsymbol{d}))(-\rho \nabla_{\boldsymbol{d}} \tilde{f}_s), \tag{61}$$

where

$$\nabla_{\boldsymbol{d}} |f_c|^2 = \nabla_{\boldsymbol{d}} f_c \times f_c^*(\boldsymbol{d}) + f_c(\boldsymbol{d}) \times \nabla_{\boldsymbol{d}}(f_c^*)$$
$$= \nabla_{\boldsymbol{d}} f_c \times f_c^*(\boldsymbol{d}) + f_c(\boldsymbol{d}) \times (\nabla_{\boldsymbol{d}} f_c)^*$$
$$\nabla_{\boldsymbol{d}} \tilde{f}_s = \nabla_{\boldsymbol{d}} |f_s|^2$$
$$= \nabla_{\boldsymbol{d}} f_s \times f_s^*(\boldsymbol{d}) + f_s(\boldsymbol{d}) \times \nabla_{\boldsymbol{d}}(f_s^*)$$
$$= \nabla_{\boldsymbol{d}} f_s \times f_s^*(\boldsymbol{d}) + f_s(\boldsymbol{d}) \times (\nabla_{\boldsymbol{d}} f_s)^*. \tag{62}$$

Similarly, $\nabla_{\boldsymbol{d}} f_c$ can be derived by (55)-(58).

APPENDIX C
COMPUTATIONAL COMPLEXITY

Since the computation of the analytic solution in subproblem (45)-(51) does not require internal iterations, most of the computing time is spent in the calculation of the objective function and its gradient in SQP algorithm for the nonconvex problems (52) and (43). For simplicity, we analyze the time complexity of the innermost function in detail. f_s (see (23)) requires about MN complex additions, which are equivalent to $2MN$ additions of real numbers. Its gradient $\nabla_d f_s$ (see (55)-(58)) requires about $2MN$ complex multiplications and $2MN$ complex additions, which are equivalent to $4MN$ multiplications, $4MN$ multiplication-addition operations, and $4MN$ additions. Therefore, the complexity of SQP algorithm is about $\mathcal{O}(14MNST_{sqp})$, where S is the number of sidelobe sampling points and T_{sqp} is the number of iterations of SQP. The total complexity of Algorithm 1 and Algorithm 2 is $\mathcal{O}(14MNST_{sqp}T)$, where T is the number of iterations of ADMM or Lagrangian multiplier method. Generally speaking, the more antennas there are, the larger S is. For example, $S = 100$ for 2T3R configuration and $S = 500$ for 1T16R configuration. The SQP algorithm usually requires 5-50 iterations to converge, and ADMM requires at least 100 iterations.

Compared with other synthesis techniques, like GA and SA-PSO, the proposed single optimization takes longer, but our methods have demonstrated an excellent searching capability, and usually a single run is sufficient to find an optimal solution with Pareto optimality, whereas other methods require at least thousands of tests, with different initializations, to find a good solution. It is worth mentioning that sparse array geometry optimization is not a task that requires to be performed in real-time: a reasonable computation time is acceptable if the achieved results are excellent [37]. Moreover, the non-uniform FFT technique will be exploited to accelerate the computation in our future work.

REFERENCES

[1] J. Li and P. Stoica, *MIMO Radar Signal Processing*. Hoboken, NJ, USA: John Wiley & Sons, Inc., Oct. 2008.

[2] S. Sun, A. P. Petropulu, and H. V. Poor, "MIMO Radar for Advanced Driver-Assistance Systems and Autonomous Driving: Advantages and Challenges," *IEEE Signal Processing Magazine*, vol. 37, no. 4, pp. 98–117, 2020.

[3] C. Waldschmidt, J. Hasch, and W. Menzel, "Automotive Radar — From First Efforts to Future Systems," *IEEE Journal of Microwaves*, vol. 1, no. 1, pp. 135–148, 2021.

[4] J. Le Kernec, F. Fioranelli, C. Ding, H. Zhao, L. Sun, H. Hong, J. Lorandel, and O. Romain, "Radar Signal Processing for Sensing in Assisted Living: The Challenges Associated With Real-Time Implementation of Emerging Algorithms," *IEEE Signal Processing Magazine*, vol. 36, no. 4, pp. 29–41, 2019.

[5] R. Schmidt, "Multiple emitter location and signal parameter estimation," *IEEE Transactions on Antennas and Propagation*, vol. 34, no. 3, pp. 276–280, Mar. 1986.

[6] W. Roberts, P. Stoica, J. Li, T. Yardibi, and F. A. Sadjadi, "Iterative Adaptive Approaches to MIMO Radar Imaging," *IEEE Journal of Selected Topics in Signal Processing*, vol. 4, no. 1, pp. 5–20, Feb. 2010.

[7] P. Rocca, G. Oliveri, R. J. Mailloux, and A. Massa, "Unconventional Phased Array Architectures and Design Methodologies—A Review," *Proceedings of the IEEE*, vol. 104, no. 3, pp. 544–560, Mar. 2016.

[8] T. I. Inc., "Design guide: TIDEP01012—Imaging radar using cascaded mmWave sensor reference design (REV. A)," http://www.ti.com/lit/ug/tiduen5a/tiduen5a.pdf, Jun. 2019.

[9] A. Moffet, "Minimum-redundancy linear arrays," *IEEE Transactions on Antennas and Propagation*, vol. 16, no. 2, pp. 172–175, Mar. 1968.

[10] N. Amani, F. Jansen, A. Filippi, M. V. Ivashina, and R. Maaskant, "Sparse Automotive MIMO Radar for Super-Resolution Single Snapshot DOA Estimation With Mutual Coupling," *IEEE Access*, vol. 9, pp. 146 822–146 829, 2021.

[11] R. Feger, C. Wagner, S. Schuster, S. Scheiblhofer, H. Jager, and A. Stelzer, "A 77-GHz FMCW MIMO Radar Based on an SiGe Single-Chip Transceiver," *IEEE Transactions on Microwave Theory and Techniques*, vol. 57, no. 5, pp. 1020–1035, May 2009.

[12] C. M. Schmid, R. Feger, C. Wagner, and A. Stelzer, "Design of a linear non-uniform antenna array for a 77-GHz MIMO FMCW radar," *IEEE MTT-S International Microwave Workshop Series on Wireless Sensing, Local Positioning and RFID, Proceedings, IMWS 2009 - Croatia*, pp. 1–4, 2009.

[13] M. Eric, A. Zejak, and M. Obradovic, "Ambiguity characterization of arbitrary antenna array: Type I ambiguity," *IEEE International Symposium on Spread Spectrum Techniques & Applications*, vol. 3, no. October, pp. 955–957, 1998.

[14] O. Lange and B. Yang, "Array geometry optimization for direction-of-arrival estimation including subarrays and tapering," in *2010 International ITG Workshop on Smart Antennas (WSA)*, Feb. 2010, pp. 135–142.

[15] ——, "Antenna geometry optimization for 2D direction-of-arrival estimation for radar imaging," in *2011 International ITG Workshop on Smart Antennas*, Feb. 2011, pp. 1–8.

[16] C. Vasanelli, R. Batra, A. Di Serio, F. Boegelsack, and C. Waldschmidt, "Assessment of a Millimeter-Wave Antenna System for MIMO Radar Applications," *IEEE Antennas and Wireless Propagation Letters*, vol. 16, pp. 1261–1264, 2017.

[17] C. Vasanelli, R. Batra, and C. Waldschmidt, "Optimization of a MIMO radar antenna system for automotive applications," *2017 11th European Conference on Antennas and Propagation, EUCAP 2017*, pp. 1113–1117, 2017.

[18] A. Di Serio, P. Hugler, F. Roos, and C. Waldschmidt, "2-D MIMO Radar: A Method for Array Performance Assessment and Design of a Planar Antenna Array," *IEEE Transactions on Antennas and Propagation*, vol. 68, no. 6, pp. 4604–4616, 2020.

[19] M. A. González-Huici, D. Mateos-Núñez, C. Greiff, and R. Simoni, "Constrained optimal design of automotive radar arrays using the Weiss-Weinstein Bound," in *2018 IEEE MTT-S International Conference on Microwaves for Intelligent Mobility (ICMIM)*, Apr. 2018, pp. 1–4.

[20] W. Roberts, L. Xu, J. Li, and P. Stoica, "Sparse Antenna Array Design for MIMO Active Sensing Applications," *IEEE Transactions on Antennas and Propagation*, vol. 59, no. 3, pp. 846–858, Mar. 2011.

[21] Z. Peng and C. Li, "A Portable K -Band 3-D MIMO Radar With Nonuniformly Spaced Array for Short-Range Localization," *IEEE Transactions on Microwave Theory and Techniques*, vol. 66, no. 11, pp. 5075–5086, Nov. 2018.

[22] D. Mateos-Nunez, M. A. Gonzalez-Huici, R. Simoni, F. B. Khalid, M. Eschbaumer, and A. Roger, "Sparse array design for automotive MIMO radar," *EuRAD 2019 - 2019 16th European Radar Conference*, pp. 249–252, 2019.

[23] R. Z. Syeda, M. C. van Beurden, and A. B. Smolders, "Sparse virtual array synthesis for MIMO radar imaging systems," *IET Microwaves, Antennas & Propagation*, vol. 15, no. 11, pp. 1458–1472, 2021.

[24] A. Gupta, U. Madhow, A. Arbabian, and A. Sadri, "Design of Large Effective Apertures for Millimeter Wave Systems Using a Sparse Array of Subarrays," *IEEE Transactions on Signal Processing*, vol. 67, no. 24, pp. 6483–6497, Dec. 2019.

[25] J. Liang, X. Zhang, H. C. So, and D. Zhou, "Sparse Array Beampattern Synthesis via Alternating Direction Method of Multipliers," *IEEE Transactions on Antennas and Propagation*, vol. 66, no. 5, pp. 2333–2345, May 2018.

[26] W. Fan, J. Liang, X. Fan, and H. C. So, "A unified sparse array design framework for beampattern synthesis," *Signal Processing*, vol. 182, p. 107930, May 2021.

[27] J. Liang, M. Huan, X. Deng, T. Bao, and G. Wang, "Optimal transmitter and receiver placement for localizing 2D interested-region target with constrained sensor regions," *Signal Processing*, vol. 183, p. 108032, 2021.

[28] S. Boyd, "Distributed Optimization and Statistical Learning via the Alternating Direction Method of Multipliers," *Foundations and Trends® in Machine Learning*, vol. 3, no. 1, pp. 1–122, 2010.

[29] S. S. Saleem, M. M. Ahmed, U. Rafique, and U. F. Ahmed, "Optimization of linear antenna array for low SLL and high directivity," in *2016 19th International Multi-Topic Conference (INMIC)*, Dec. 2016, pp. 1–6.

[30] M. Viberg and C. Engdahl, "Element position considerations for robust direction finding using sparse arrays," in *Conference Record of the Thirty-Third Asilomar Conference on Signals, Systems, and Computers (Cat. No.CH37020)*, vol. 2, 1999, pp. 835–839 vol.2.

[31] C. Vasanelli, F. Roos, A. Durr, J. Schlichenmaier, P. Hugler, B. Meinecke, M. Steiner, and C. Waldschmidt, "Calibration and Direction-of-Arrival Estimation of Millimeter-Wave Radars: A Practical Introduction," *IEEE Antennas and Propagation Magazine*, vol. 62, no. 6, pp. 34–45, 2020.

[32] M. Plotkin, "Beamwidth of Phased Arrays," *IEEE Transactions on Antennas and Propagation*, vol. 21, no. 5, pp. 695–697, 1973.

[33] S. K. Singh, V. B. Chandrudu, and G. K. Mahanti, "Synthesis of linear array antenna for fixed level of side lobe level and first null beam width using particle swarm optimization," in *2013 International Conference on Communication and Signal Processing*, Apr. 2013, pp. 275–279.

[34] K. Chen, Z. He, and C. Han, "A modified real GA for the sparse linear array synthesis with multiple constraints," *IEEE Transactions on Antennas and Propagation*, vol. 54, no. 7, pp. 2169–2173, Jul. 2006.

[35] A. Azremi, M. Costa, V. Koivunen, and P. Vainikainen, "Ambiguity analysis of isolation - based multi-antenna structures on mobile terminal," in *Proceedings of the 5th European Conference on Antennas and Propagation (EUCAP)*, Apr. 2011, pp. 552–556.

[36] R. L. Haupt, *Antenna Arrays: A Computational Approach*. Hoboken, NJ, USA: John Wiley & Sons, Inc., Mar. 2010.

[37] D. Pinchera, M. D. Migliore, and G. Panariello, "Isophoric Inflating Deflating Exploration Algorithm (I-IDEA) for Equal-Amplitude Aperiodic Arrays," *IEEE Transactions on Antennas and Propagation*, vol. 70, no. 11, pp. 10 405–10 416, Nov. 2022.

[38] A. Durr, D. Schwarz, S. Hafner, M. Geiger, F. Roos, M. Hitzler, P. Hugler, R. Thoma, and C. Waldschmidt, "High-Resolution 160-GHz Imaging MIMO Radar Using MMICs With On-Chip Frequency Synthesizers," *IEEE Transactions on Microwave Theory and Techniques*, vol. 67, no. 9, pp. 3897–3907, 2019.

[39] J. Nocedal and S. J. Wright, *Numerical Optimization Second Edition*. World Scientific, 1999.

[40] J. S. Arora, "Chapter 18 - Multi-objective Optimum Design Concepts and Methods," in *Introduction to Optimum Design (Fourth Edition)*. Boston: Academic Press, Jan. 2017, pp. 771–794.

[41] J. Liang, X. Fan, H. C. So, and D. Zhou, "Array Beampattern Synthesis Without Specifying Lobe Level Masks," *IEEE Transactions on Antennas and Propagation*, vol. 68, no. 6, pp. 4526–4539, Jun. 2020.

[42] J. R. James and P. S. Hall, *Handbook of Microstrip Antennas*. Peter Peregrinus, 1989.

[43] X. He, C. Alistarh, and S. K. Podilchak, "Optimal MIMO Sparse Array Design Based on Simulated Annealing Particle Swarm Optimization," in *2022 16th European Conference on Antennas and Propagation (EuCAP)*, Mar. 2022, pp. 1–5.

[44] H. Krim and M. Viberg, "Two decades of array signal processing research: The parametric approach," *IEEE Signal Processing Magazine*, vol. 13, no. 4, pp. 67–94, Jul. 1996.

[45] D. Han and X. Yuan, "A Note on the Alternating Direction Method of Multipliers," *Journal of Optimization Theory and Applications*, vol. 155, no. 1, pp. 227–238, Oct. 2012.

Junli Liang (SM'16) was born in China. He received the Ph.D. degree in signal and information processing from the Chinese Academy of Sciences, Beijing, China, in 2007. He is currently a Professor with the School of Electronics and Information, Northwestern Polytechnical University, Xi'an, China. His research interests include radar signal processing, machine learning, 6G, and their applications.

Yifan Wu was born in China. He is currently working toward the Ph.D. degree with the School of Electronics and Information, Northwestern Polytechnical University, Xi'an, China. His research focuses on radar signal processing and its application.

Yongkang Li was born in Hunan, China. He received the B.Eng. degree in electronic information engineering and the Ph.D. degree in signal and information processing from Xidian University, Xi'an, China, in 2011 and 2016, respectively. From Aug. 2015 to Aug. 2016, he was a visiting researcher with the School of Electrical and Electronic Engineering, Nanyang Technological University, Singapore. Since Jun. 2022, he has been an associate professor with the School of Electronics and Information, Northwestern Polytechnical University, China. His research interest is radar signal processing.

Mingsai Huan was born in Weifang, China, in 1996. He is currently working toward the Ph.D. degree with the School of Electronics and Information, Northwestern Polytechnical University, Xi'an, China. His research focuses on sparse arrays and their applications in automotive radar and indoor radar sensors.

Wei Liu (S'01-M'04-SM'10) received his BSc and LLB. degrees from Peking University, China, in 1996 and 1997, respectively, MPhil from the University of Hong Kong in 2001, and PhD from University of Southampton, UK, in 2003. He then worked as a postdoc first at Southampton and later at Imperial College London. Since September 2005, he has been with the Department of Electronic and Electrical Engineering, University of Sheffield, UK, first as a Lecturer and then a Senior Lecturer. He has published 380+ journal and conference papers, five book chapters, and two research monographs titled "Wideband Beamforming: Concepts and Techniques" (Wiley, March 2010) and "Low-Cost Smart Antennas" (Wiley, March 2019), respectively. His research interests cover a wide range of topics in signal processing, with a focus on sensor array signal processing and its various applications, such as robotics and autonomous systems, human computer interface, radar, sonar, and wireless communications.

He is a member of the Digital Signal Processing Technical Committee of the IEEE Circuits and Systems Society (Chair from May 2022) and the Sensor Array and Multichannel Signal Processing Technical Committee of the IEEE Signal Processing Society (Chair for 2021-2022). He was an Associate Editor for IEEE Trans. on Signal Processing (2015-2019) and IEEE Access (2016-2021), and is currently an editorial board member of the journals Frontiers of Information Technology and Electronic Engineering and Journal of the Franklin Institute.